Electronic supplementary information for:

Photocatalytic hydrogen evolution over nickel cobalt bimetallic phosphate anchored graphitic carbon nitrides by regulation of d-band electronic structure

Yuanzheng Zhang [a], Yunrong Dai [b,c], Lifeng Yin [a,c,*], Huihui Li [a], Xiang Chen [a], and Bin Chen [a*]

a State Key Laboratory of Water Environment Simulation, School of Environment, Beijing Normal Univ

b School of Water Resources and Environment, China University of Geosciences (Beijing), Beijing, PR China;

c Division of Engineering and Applied Science, Linde-Robinson Laboratory, California Institute of Technology, Pasadena, California, 91125, USA.

* Corresponding author.

E-mail address: chenb@bnu.edu.cn (B. Chen), lfyin@bnu.edu.cn (L. Yin)

Table S1. Summary of non-noble based cocatalysts for photocatalyst hydrogen evolution.

Photocatalyst	cocatalyst	Reaction condition	Light source	H_2 evolution ($\mu mol\ h^{-1}g^{-1}cat$)	Ref.
CdS	MoO_x	20 vol% lactic	$\lambda > 400$ nm	2868	1
MIL-125-NH_2	NiO/Ni_2P	16 vol% TEA	$\lambda > 420$ nm	1084/1230	2
$SrTiO_3$	Ni@NiO_x	Pure water	$\lambda > 300$ nm	~18	3
g-C_3N_4	Mo-Mo_2C	20 vol% TEOA	$\lambda > 420$ nm	219.7	4
g-C_3N_4	Ni_2P@BP	10 vol% TEOA	$\lambda > 420$ nm	858.2	5
g-C_3N_4	Ni-Mo	10 vol% TEOA	$\lambda > 420$ nm	1785	6
g-C_3N_4	NiO	10 vol% TEOA	$\lambda > 420$ nm	68.8	7
g-C_3N_4	Ni_2P	10 vol% TEOA	$\lambda > 420$ nm	82.5	8
g-C_3N_4	Ni_3C	15 vol% TEOA	$\lambda > 420$ nm	303.6	9
g-C_3N_4	CoP	15 vol% TEOA	$\lambda > 420$ nm	1924	10
g-C_3N_4	CoS_x	20 vol% TEOA	$\lambda > 400$ nm	629	11
sg-CN	Ni_2P	10 vol% TEOA	$\lambda > 420$ nm	330	12
g-C_3N_4	NiCoP@NiCo–Pi	10 vol% TEOA	$\lambda > 420$ nm	534.2	13
g-C_3N_4	NiCo-Pi	10 vol% TEOA	$\lambda = 410$ nm	10184	This work

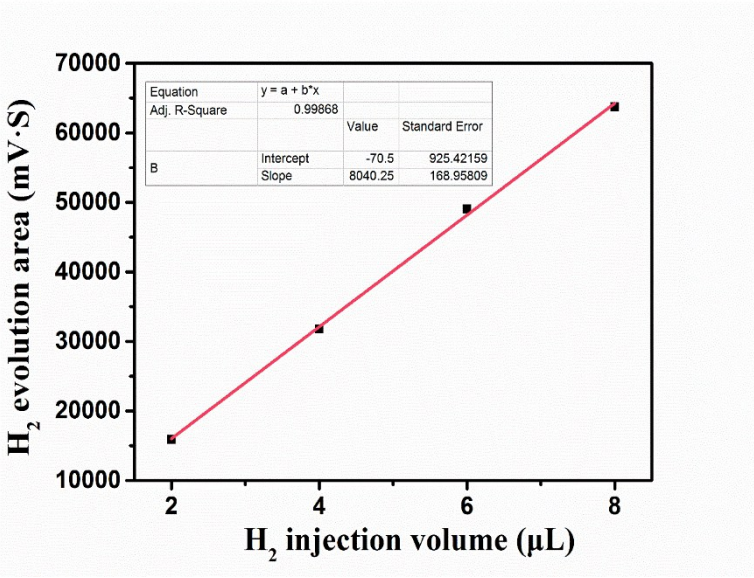

Fig. S1. Standard curve for H_2 established by gas chromatography. The inset shows the corresponding fitting information.

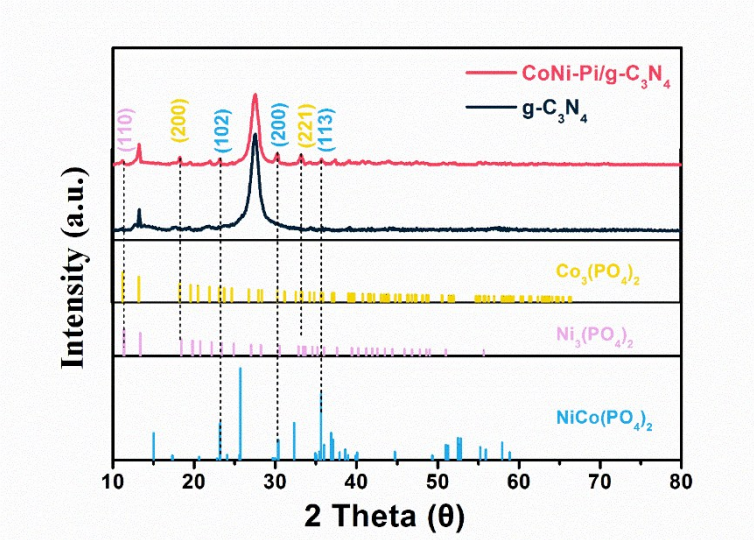

Fig. S2. X-ray diffraction (XRD) patterns of g-C_3N_4 and NiCo-Pi/g-C_3N_4. There are some new diffraction peaks (blue color) on the NiCo-Pi/g-C_3N_4, which can be mainly assigned to $CoNi(PO_4)_2$, indicating that the formation of NiCo-Pi solid solution. The diffraction peaks (pink and yellow) can be mainly assigned to $Co_3(PO_4)_2$ (PDF#41-0375) and $Ni_3(PO_4)_2$ (PDF#33-0951).

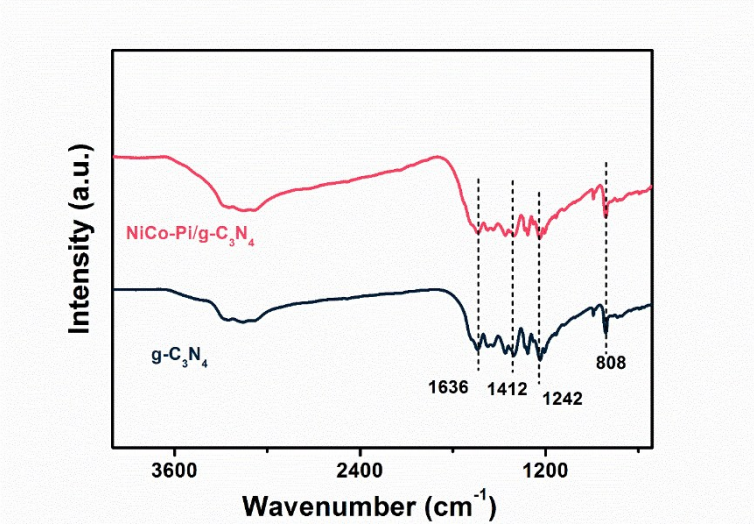

Fig. S3. Fourier transform infrared (FT-IR) spectra of g-C_3N_4 and NiCo-Pi/g-C_3N_4.

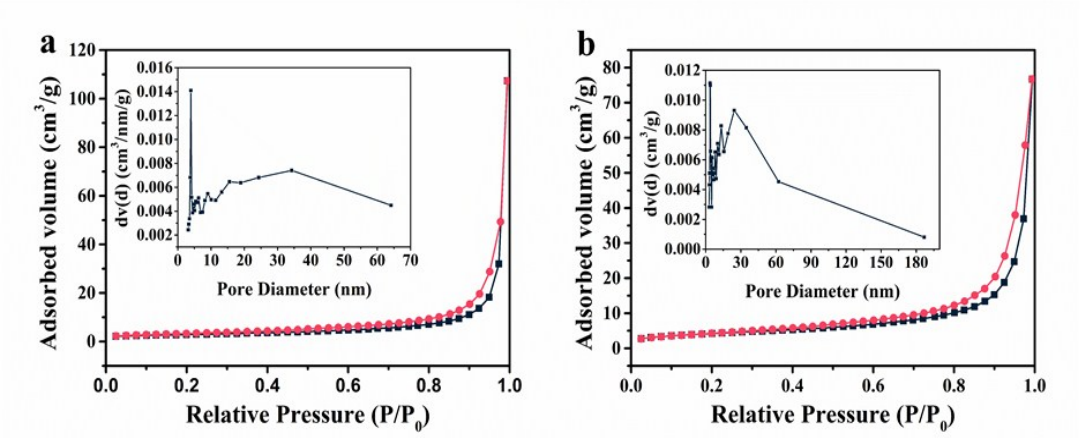

Fig. S4. (a) N_2 adsorption–desorption isotherms and the corresponding pore distribution curves of g-C_3N_4 (inset); (b) N_2 adsorption–desorption isotherms and the corresponding pore distribution curves of NiCo-Pi/g-C_3N_4 (inset).

The Brunauer-Emmett-Teller (BET) surface area and the Barret-Joyner-Halenda (BJH) pore size distribution of the samples were obtained from the N_2 adsorption-desorption measurements. The N_2 adsorption-desorption isotherms of the g-C_3N_4 and NiCo-Pi/g-C_3N_4 samples are type IV with H3-type hysteresis loops ($0.8 < P/P_0 < 1.0$), indicating the presence of mesoporous and macropores.[14] The BET surface area of NiCo-Pi/g-C_3N_4 was calculated to be 79.5 $m^2\ g^{-1}$, which is much higher than that of g-C_3N_4 (57.6 $m^2\ g^{-1}$). Additionally, the pore size distribution curve of g-C_3N_4 exhibits a sharp peak at 3.9 nm, while the pore size distribution of NiCo-Pi/g-C_3N_4 is widely distributed between 0-30 nm.

Table S2. Textural properties of the pure g-C_3N_4 and NiCo-Pi/g-C_3N_4 composite.

Sample	Surface area (m^2g^{-1})	Pore size (nm)	Pore volume ($cm^3\ g^{-1}$)
g-C_3N_4	57.6	19.7	0.205
NiCo-Pi/g-C_3N_4	79.5	18.1	0.302

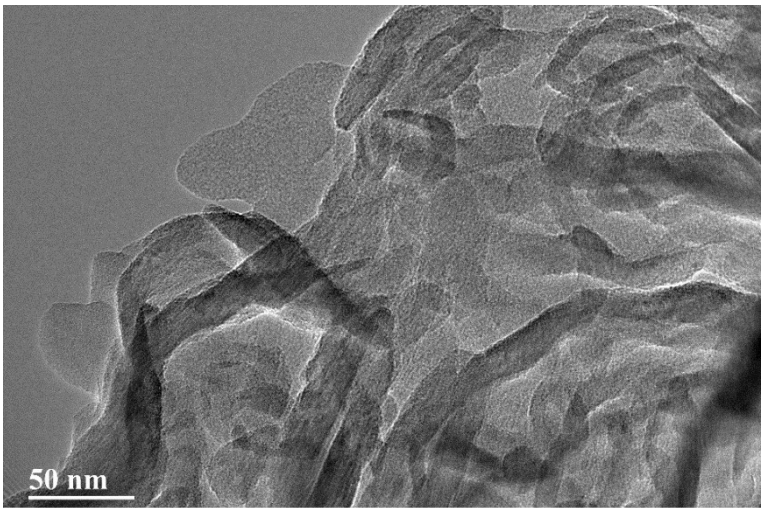

Fig. S5. Transmission electron microscopy (TEM) image of as-prepared g-C_3N_4 with layer by layer structures.

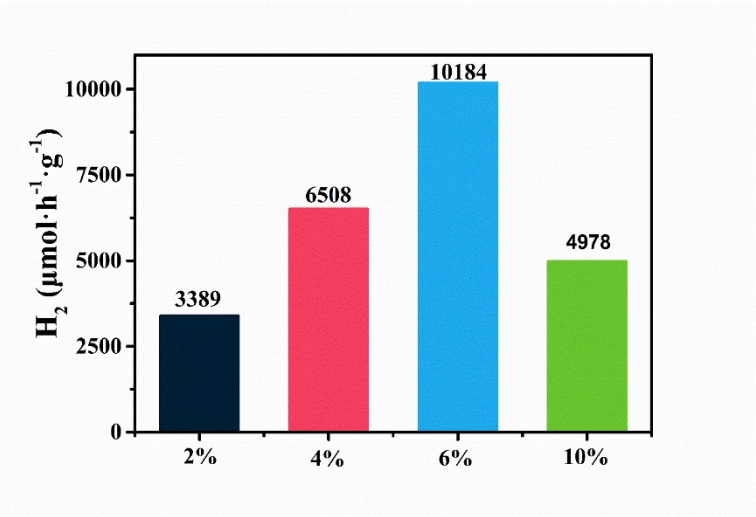

Fig. S6. Photocatalytic H_2 evolution rate of NiCo-Pi/g-C_3N_4 composites (Ni/Co molar ratio of 4:5) with different NiCo-Pi contents (2 wt%, 4 wt%, 6 wt%, 10 wt%) under visible light. The H_2 evolution rate increased from 2 wt% to 6 wt%, and decreased thereafter, probably because the excess of NiCo-Pi resulted in the shielding of the active sites on the catalyst surface and reduced the light penetration depth in the reaction solution.

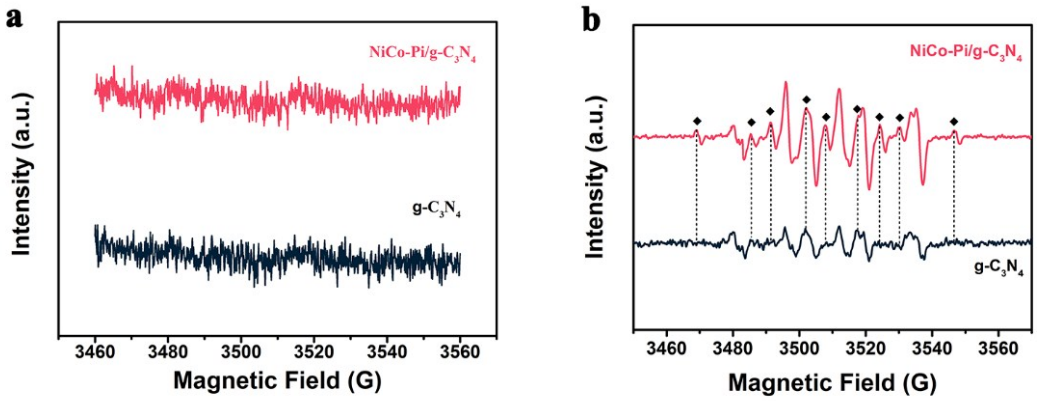

Fig. S7. (a) DMPO adducts recorded in the binary systems containing H_2O and catalyst under visible light (λ□420 nm) .(b) DMPO adducts recorded in the ternary systems containing H_2O, TEOA and catalyst (◆:- DMPO-•H) under visible light (λ□420 nm). As shown in the Fig. S7a, no free radicals were detected in pure water, indicating that the redox reaction of water would not occur. It is worth noting that hydrogen radicals (·H) are trapped in the presence of sacrificial agents,[15,16] and the signal strength of NiCo-Pi/g-C_3N_4 is significantly stronger than that of the original g-C_3N_4 (Fig. S7b), which indicates that NiCo-Pi can indeed promote the proton reduction reaction.

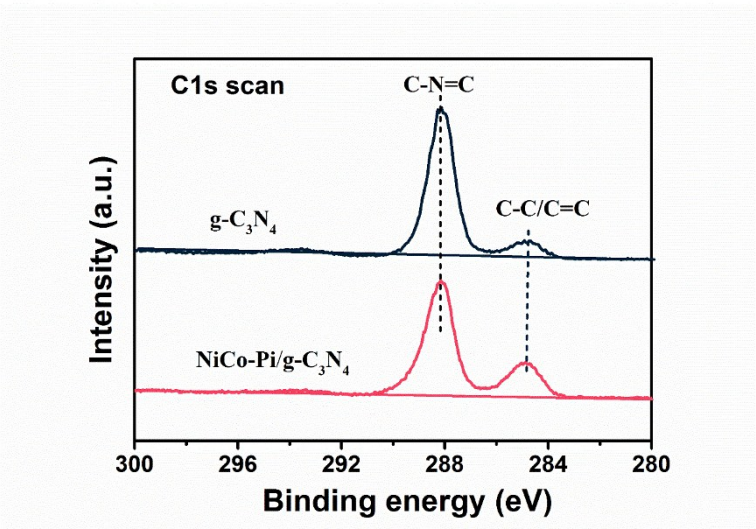

Fig. S8. C 1s XPS spectra of g-C_3N_4 and NiCo-Pi/g-C_3N_4. The C1s spectra can be differentiated into two peaks at 288.2 eV and 284.8 eV, which are ascribed to the C–N=C of the g-C_3N_4 and C–C/C=C groups, respectively.[17]

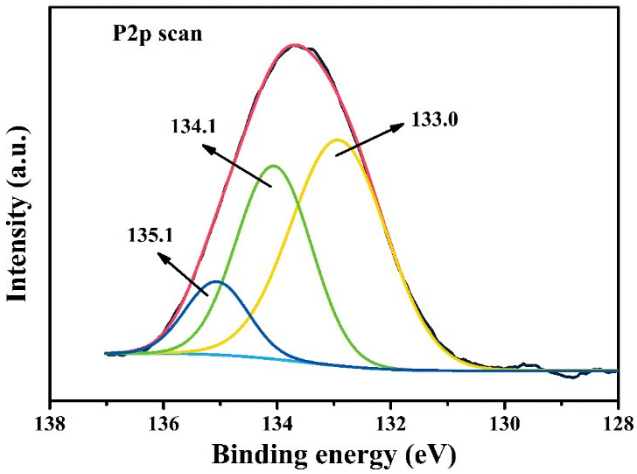

Fig. S9. P 2p XPS spectra of NiCo-Pi/g-C_3N_4.

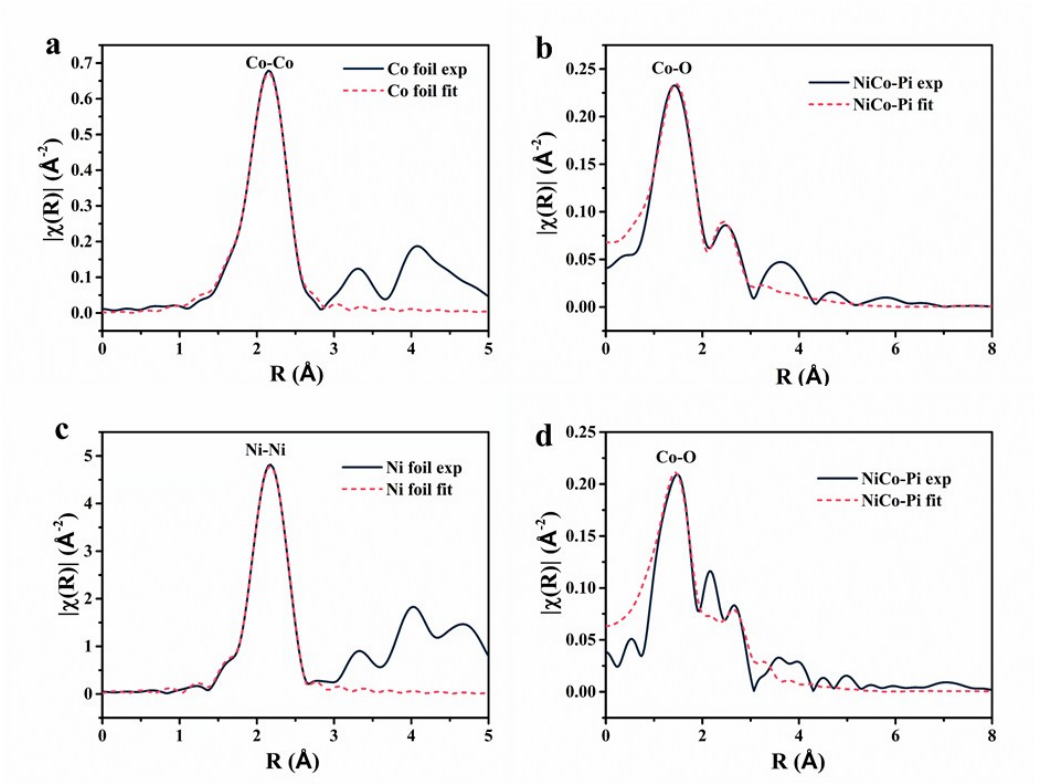

Fig. S10. Fourier transform magnitude of Co K-edge EXAFS spectra in R space for (a) Co foil, and (b) NiCo-Pi (not corrected for phase shift). Fourier transform magnitude of Ni K-edge EXAFS spectra in R space for (c) Ni foil, and (d) NiCo-Pi (not corrected for phase shift).

Table S3. Co K-edge EXAFS curve Fitting Parameters[a]

Sample	shell	N	R (Å)	$\sigma^2\times10^{-3}$ (Å^2)	ΔE_0 (eV)	R factor
Co foil[b]	Co-Co	12	2.49	6.1	0.7	0.003
NiCo-Pi[c]	Co-O	4.6	2.05	10.9	-7.6	0.005
	Co-Co/Ni	2.7	3.01			
NiCo-Pi/g-C_3N_4[d]	Co-N/O	6.0	2.05	10.1	-1.9	0.002
	Co-Co/Ni	1.9	3.01			

Table S4. Ni K-edge EXAFS curve Fitting Parameters[a]

Sample	shell	N	R (Å)	$\sigma^2\times10^{-3}$ (Å^2)	ΔE_0 (eV)	R factor
Ni foil[e]	Ni-Ni	12	2.48	6.0	7.1	0.003
NiCo-Pi[f]	Ni-O	8.3	2.03	9.5	-8.4	0.003
	Ni-Co/Ni	3.4	3.46			
NiCo-Pi/g-C_3N_4[g]	Ni-N/O	7.7	2.00	12.0	-11.7	0.018
	Ni-Co/Ni	5.7	3.42			

[a] N, coordination number; R, distance between absorber and backscatter atoms; σ^2, Debye–Waller factor to account for both thermal and structural disorders; ΔE_0, inner potential correction; R factor indicates the goodness of the fit. Error bounds (accuracies) that characterize the structural parameters obtained by EXAFS spectroscopy were estimated as N ± 20%; R ± 1%; σ^2 ± 20%; ΔE_0 ± 20%. Bold numbers indicate a fixed coordination number (N) according to the crystal structure. [b] Fitting range: 3.0 ≤ k (/Å) ≤ 12.5 and 1.0 ≤ R (Å) ≤ 3.0. [c] Fitting range: 3.0 ≤ k (/Å) ≤ 8.0 and 1.0 ≤ R (Å) ≤ 3.0. [d] Fitting range: 3.0 ≤ k (/Å) ≤ 8.0 and 1.0 ≤ R (Å) ≤ 3.1. [e] Fitting range: 3.0 ≤ k (/Å) ≤ 12.5 and 1.0 ≤ R (Å) ≤ 3.0. [f] Fitting range: 3.0 ≤ k (/Å) ≤ 10.0 and 1.0 ≤ R (Å) ≤ 3.0. [g] Fitting range: 3.0 ≤ k (/Å) ≤ 10.0 and 1.0 ≤ R (Å) ≤ 3.0.

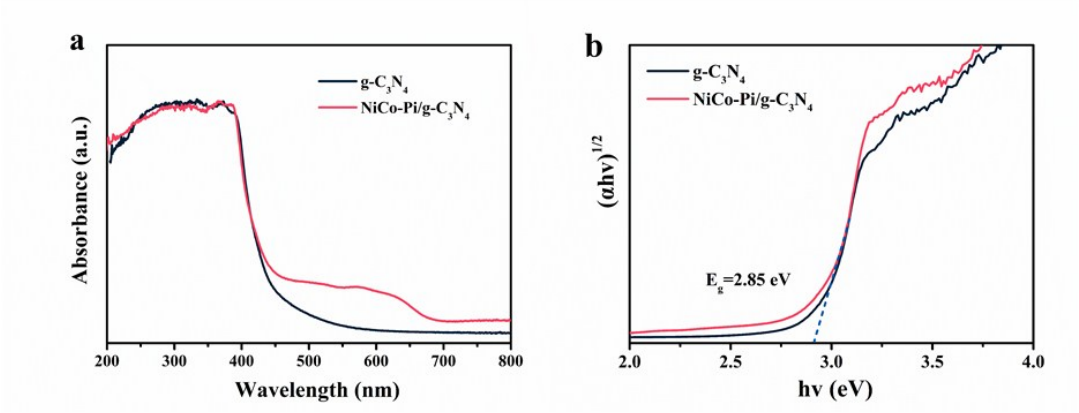

Fig. S11. (a) UV–visible adsorption spectra and (b) $(\alpha h\nu)^{1/2}$ versus hν curves of g-C_3N_4 and NiCo-Pi/g-C_3N_4. Both samples exhibited the characteristic absorption at approximately 380 nm, which is assigned to π-π* transitions normally seen in heterocyclic aromatics of g-C_3N_4.[18] The derived electronic band gaps of g-C_3N_4 and NiCo-Pi/g-C_3N_4 can be calculated according to the Tauc plots:

$$\alpha h\upsilon = A(h\upsilon\text{-}E_g)^{n/2}$$

where h is the Planck constant, υ is the light frequency, A is a constant, α is the absorption coefficient, and E_g is the band gap. The variable number n value of g-C_3N_4 is 1 due to its direct-allowed transition.[19,20]

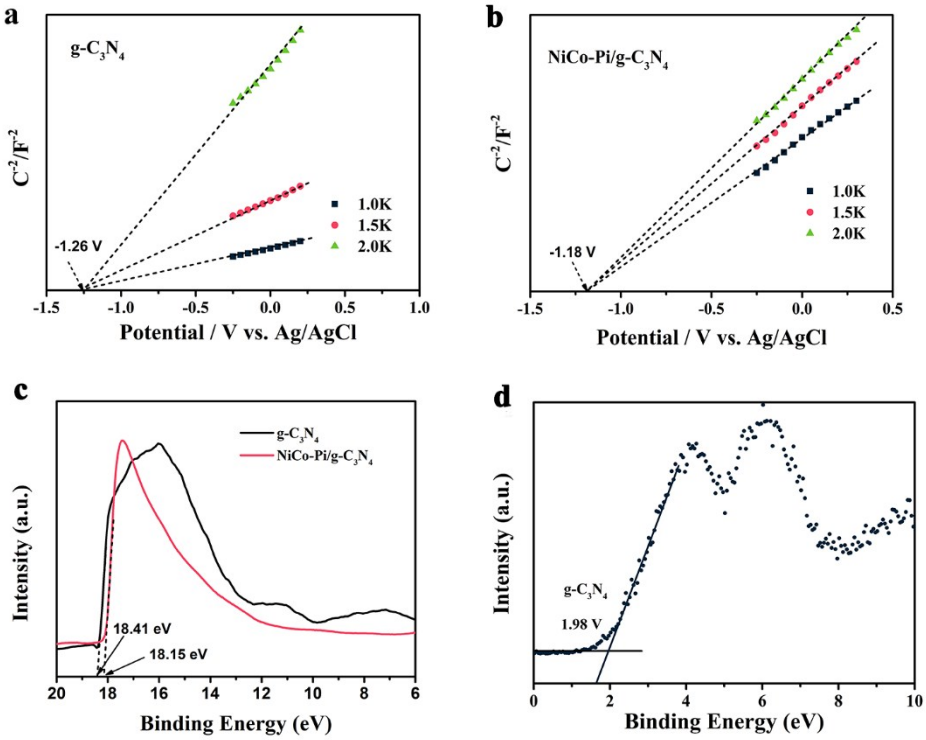

Fig. S12. (a) Mott-Schottky plots of g-C_3N_4, (b) NiCo-Pi/g-C_3N_4. (c) UPS spectra of g-C_3N_4 and NiCo-Pi/g-C_3N_4. (d) VB XPS of g-C_3N_4.

Table S5. Parameters of equivalent circuit for the impedance data of the prepared samples.

Sample	Rs (Ω)	Rct (kΩ)
g-C_3N_4	124	257
NiCo-Pi/g-C_3N_4 (Ni:Co=0:1)	25.5	188
NiCo-Pi/g-C_3N_4 (Ni:Co=1:3)	49.4	25.9
NiCo-Pi/g-C_3N_4 (Ni:Co=2:3)	50	15
NiCo-Pi/g-C_3N_4 (Ni:Co=4:5)	126	12.1
NiCo-Pi/g-C_3N_4 (Ni:Co=1:1)	119	11.9
NiCo-Pi/g-C_3N_4 (Ni:Co=0:1)	66.2	166

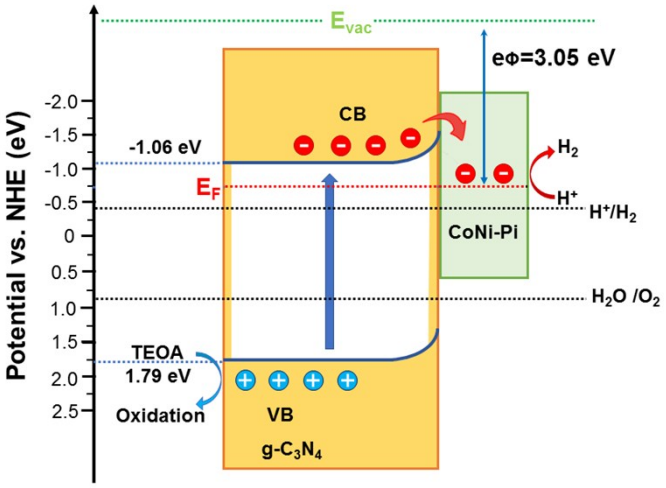

Fig. S13. Energy band configuration and photo-induced charge generation/transfer process in NiCo-Pi/g-C_3N_4 during visible light photocatalytic H_2 evolution. E_F: Fermi level; E_{vac}: vacuum energy; e_Φ: work functions

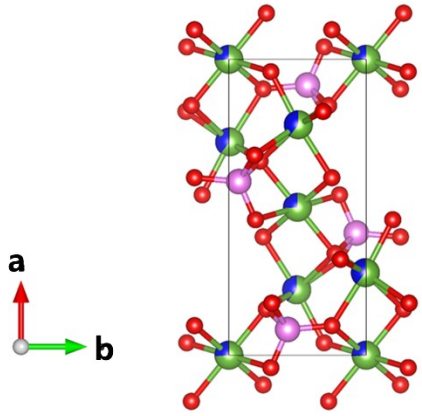

Fig. S14. The ball-and-stick model of $(Ni_{0.65}Co_{0.35})_3(PO_4)_2$. The $(Ni_{0.65}Co_{0.35})_3(PO_4)_2$ crystallized in the monoclinic system with the lattice constants a= 10.185(4) Å, b= 4.713(3) Å, c= 5.865(2) Å.[21] The green, blue, red and violet balls represent Ni, Co, O, and P atoms, respectively. All the NiCo-Pi crystal structures with different Ni/Co molar ratios were geometrically optimized based on the above configuration.

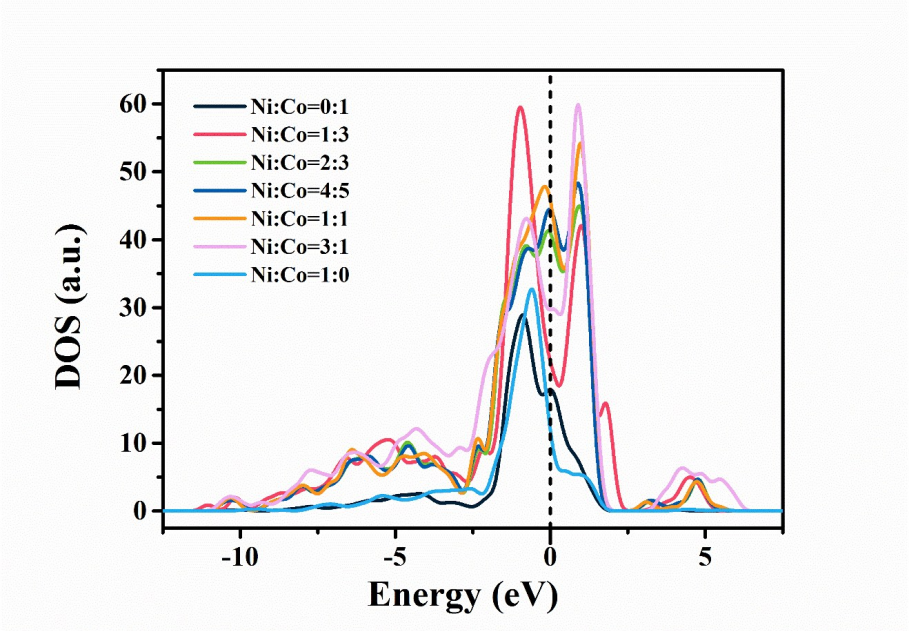

Fig. S15. d-band density of states for NiCo-Pi with different Ni/Co molar ratios. The black dashed line denotes the position of the Fermi level.

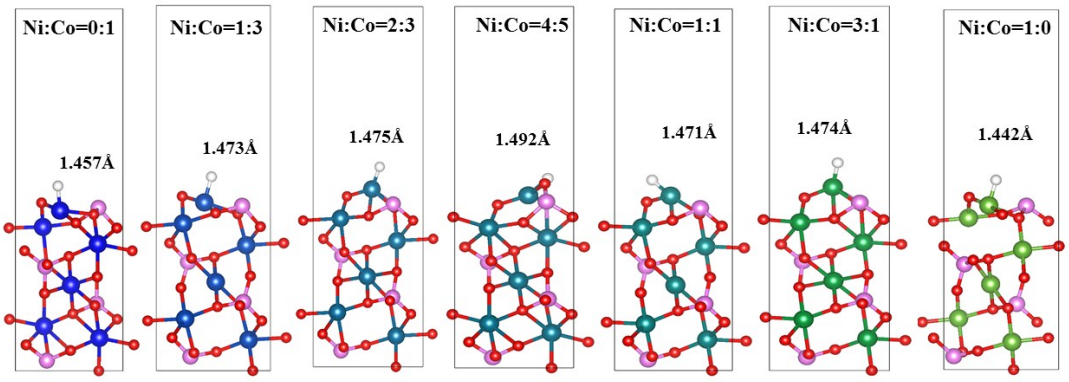

Fig. S16. Optimized geometry structures for H atom adsorption on surface of NiCo-Pi with different Ni/Co molar ratios. The white, red, violet and other colors represent H, O, P and Ni/Co atoms, respectively.

References

1. H. Zhang, P. Zhang, M. Qiu, J. Dong and X. W. Lou, *Adv. Mater.*, 2018, 1804883.
2. S. Kampouri, T. N. Nguyen, M. Spodaryk, R. G. Palgrave, A. Züttel, B. Smit and K. C. Stylianou, *Adv. Funct. Mater.*, 2018, **28**, 1806368.
3. K. Han, T. Kreuger, B. Mei and G. Mul, *ACS Catal.*, 2017, **7**, 1610-1614.
4. J. Dong, Y. Shi, C. Huang, Q. Wu, T. Zeng and W. Yao, *Appl. Catal., B* 2019, **243**, 27-35.
5. R. Boppella, W. Yang, J. Tan, H.-C. Kwon, J. Park and J. Moon, *Appl. Catal., B* 2019, **242**, 422-430.
6. X. Han, D. Xu, L. An, C. Hou, Y. Li, Q. Zhang and H. Wang, *Appl. Catal., B* 2019, **243**, 136-144.
7. J. Liu, Q. Jia, J. Long, X. Wang, Z. Gao and Q. Gu, *Appl. Catal., B* 2018, **222**, 35-43.
8. Y. Ping, X. Liu, J. Iocozzia, Y. P. Yuan, L. Gu, G. Xu and Z. Lin, *J. Mater. Chem. A*, 2017, **5**.
9. K. He, J. Xie, Z.-Q. Liu, N. Li, X. Chen, J. Hu and X. Li, *J. Mater. Chem. A*, 2018, **6**, 13110-13122.
10. C. Li, Y. Du, D. Wang, S. Yin, W. Tu, Z. Chen, M. Kraft, G. Chen and R. Xu, *Adv. Funct. Mater.*, 2017, **27**, 1604328.
11. J. Fu, C. Bie, B. Cheng, C. Jiang and J. Yu, *ACS Sustain. Chem. Eng.*, 2018, **6**, 2767-2779.
12. A. Indra, A. Acharjya, P. W. Menezes, C. Merschjann, D. Hollmann, M. Schwarze, M. Aktas, A. Friedrich, S. Lochbrunner, A. Thomas and M. Driess, *Angew. Chem. Int. Ed. Engl.*, 2017, **56**, 1653-1657.
13. Z. Qin, Y. Chen, Z. Huang, J. Su and L. Guo, *J. Mater. Chem. A*, 2017, **5**, 19025-19035.
14. J. Fu, B. Zhu, C. Jiang, B. Cheng, W. You and J. Yu, *Small*, 2017, **13**, 1603938.
15. R. Li, X. Zhu, X. Yan, H. Kobayashi, S. Yoshida, W. Chen, L. Du, K. Qian, B. Wu, S. Zou, L. Lu, W. Yi, Y. Zhou and J. Fan, ACS Catal., 2017, 7, 1478-1484.
16. L. Zhao, Q. Meng, X. Fan, C. Ye, X. Li, B. Chen, V. Ramamurthy, C. Tung, *Angew. Chem. Int. Ed. Engl.* 2017, 56, 3020-3024.
17. K. Li, Y.-Z. Lin, Y. Zhang, M.-L. Xu, L.-W. Liu and F.-T. Liu, *J. Mater. Chem. C*, 2019, **7**, 13211-13217.
18. A. B. Jorge, D. J. Martin, M. T. S. Dhanoa, A. S. Rahman, N. Makwana, J. Tang, A. Sella, F. Corà, S. Firth, J. A. Darr and P. F. McMillan, *J. Phys. Chem. C*, 2013, **117**, 7178-7185.
19. H. Yu, R. Shi, Y. Zhao, T. Bian, Y. Zhao, C. Zhou, G. I. N. Waterhouse, L. Z. Wu, C. H. Tung and T. Zhang, *Adv. Mater.*, 2017, **29**, 1605148.
20. Q. Liang, Z. Li, Z.-H. Huang, F. Kang and Q.-H. Yang, *Adv. Funct. Mater.*, 2015, **25**, 6885-6892.
21. A. G. Nord, *Zeitschrift Für Kristallographie*, 1984, **166**, 159-176.